Heliyon 9 (2023) e17748

Contents lists available at ScienceDirect

Heliyon

journal homepage: www.cell.com/heliyon

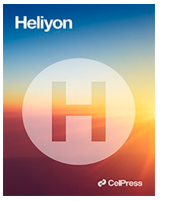

Influence of metal salts (Al, Ca, and Mg) on the work function and hole extraction at carbon counter electrodes in perovskite solar cells

Muna Fathiah Don [a], Piyasiri Ekanayake [a,b,*], James Robert Jennings [a,b], Hideki Nakajima [c], Udaya Kumar D [d], Chee Ming Lim [e]

[a] Faculty of Science, Universiti Brunei Darussalam, Jalan Tungku Link, Gadong BE 1410, Brunei Darussalam
[b] Optoelectronic Device Research Group, Universiti Brunei Darussalam, Jalan Tungku Link, Gadong BE 1410, Brunei Darussalam
[c] Synchrotron Light Research Institute, 111 University Avenue, Muang District, Nakhon Ratchasima 30000, Thailand
[d] Department of Chemistry, National Institute of Technology Karnataka, Surathkal, India
[e] Centre for Advanced Material and Energy Sciences, Universiti Brunei Darussalam, Jalan Tungku Link, Gadong BE 1410, Brunei Darussalam

ARTICLE INFO

Keywords:
Perovskite solar cells
Carbon counter electrodes
Graphite
Carbon black
Metal salts
Work function tuning
Energy level alignment

ABSTRACT

Hole transport material-free carbon-based perovskite solar cells (HTM-free *C*–PSCs) are recognized as a cost-effective and stable alternative to conventional perovskite solar cells. However, the significant energy level misalignment between the perovskite layer and the carbon counter electrode (CE) results in ineffective hole extraction and unfavorable charge recombination, which decreases the power conversion efficiency (PCE). Here, we report the introduction of metal salts (Al, Ca, and Mg) into graphite/carbon black (Gr/CB) CEs to modify the work function and enhance the hole selectivity of the CE. This modification leads to improved energy level alignment, efficient hole extraction, and reduced charge recombination. The PCE of the HTM-free *C*-PSC based on Al-modified Gr/CB as the CE material reached 9.91%, which is approximately 12% higher than that of devices employing unmodified Gr/CB CEs. This work demonstrates that by directly incorporating metal salts into the Gr/CB CE, the energy level alignment and hole extraction at the perovskite/carbon interface can be improved. This presents a viable method for enhancing the PCE of HTM-free *C*–PSCs.

1. Introduction

Hybrid organic-inorganic perovskite solar cells (PSCs) are among the most promising emerging photovoltaic technologies for converting light energy into electrical energy. The perovskite absorbers exhibit extraordinary optoelectronic properties, including a high absorption coefficient, direct optical bandgap, low exciton binding energy, long carrier diffusion length, and ambipolar charge transport. Additionally, their compatibility with simple and cost-effective manufacturing processes, such as solution processing, has enabled the power conversion efficiency (PCE) of PSCs to increase from 3.8% to 25.7%, while remaining economically viable [1–4].

However, despite the promising features of PSCs, certain issues are still preventing their commercialization. These issues include the poor stability of the perovskite layer with respect to temperature, moisture, and oxygen, the expensive hole transporting materials

* Corresponding author. Faculty of Science, Universiti Brunei Darussalam, Jalan Tungku Link, Gadong BE 1410, Brunei Darussalam.
E-mail address: piyasiri.ekanayake@ubd.edu.bn (P. Ekanayake).

https://doi.org/10.1016/j.heliyon.2023.e17748
Received 31 January 2023; Received in revised form 23 June 2023; Accepted 27 June 2023
Available online 28 June 2023

(HTM) such as spiro-OMeTAD, P3HT, and PTAA, as well as the use of noble metal counter electrodes (CEs) such as Au and Ag. Moreover, the energy-intensive processes employed during device fabrication are costly and unsuitable for mass production [5–10].

To reduce the materials cost of PSCs while addressing the limitation of poor device stability, carbon-based materials have emerged as promising candidates for the CE due to their low-cost, ease of fabrication, abundance, good electrical and thermal conductivity, as well as tunable energy levels. In addition, the hydrophobicity, chemical inertness, and typically high thickness of carbon layers employed as CEs mean that the carbon layer can serve as a barrier to prevent water from accessing the perovskite layer [11,12]. Motivated by these characteristics, extensive research has been conducted on carbonaceous materials, including carbon black [13–15], carbon nanotubes [16,17], carbon ink [18], commercial carbon paste [19], spongy carbon [20], and graphite [21,22], as replacement for expensive HTMs and noble metal CEs.

To date, the PCE values of HTM-free *C*–PSCs are still lower than those achieved by "conventional" PSCs employing metal-based CEs. This discrepancy can be attributed, in part, to the insufficient charge extraction and mismatched band alignment at the interface between the perovskite and carbon CEs, which is a common issue for HTM-free *C*–PSCs. The energy level mismatch, specifically the difference in energy between the valence band maximum (VBM) of the perovskite and the work function (WF) of the carbon CE, hampers the efficient transfer of holes from the perovskite absorber layer to the carbon CE. This reduction in hole extraction efficiency leads to severe charge recombination and ultimately results in a significant drop in PCE [23–25].

To overcome these challenges, it is crucial to optimize the WF of the carbon CE to improve device performance and facilitate more efficient hole extraction at the perovskite/carbon CE interface. Studies have demonstrated that the electrical properties of carbon materials, including the WF, can be effectively modulated by the addition of metal salts or nanoparticles [26]. One of the most successful approaches for manipulating hole extraction by carbon is the element doping method [12,27,28]. The incorporation of metal dopants into the carbon structure is recognized as an efficient technique for improving the electrical conductivity of carbon, strengthening the interfacial contact, and enhancing the energy level alignment between carbon CEs and perovskite absorber layers. This, in turn, contributes to improved charge transfer and reduced recombination losses [14,25,29,30].

In this paper, we present our discovery that graphite/carbon black (Gr/CB) CEs modified with various metal salts (Al, Ca and Mg) exhibit higher WFs compared to pristine Gr/CB CEs. We demonstrate that this phenomenon can be utilized to enhance hole extraction from perovskite absorber layers using metal-Gr/CB CEs, leading to improved PCEs and fill factors for HTM-free *C*–PSCs. Furthermore, we reveal that the introduction of metal salts into Gr/CB significantly enhances its electrical conductivity, which further benefits device performance. To the best of our knowledge, our findings represent the first example of WF tuning of Gr/CB CEs through metal salt modification. Additionally, no previous research has investigated the interfacial charge transfer between perovskite and metal-Gr/CB materials.

2. Experimental section

2.1. Materials

Fluorine-doped tin oxide coated glass substrates (FTO; sheet resistance 12 Ω/sq, Solaronix), absolute ethanol (>99%, Sigma-Aldrich), N, *N*-dimethyl formamide (DMF, 99.7%), dimethyl sulfoxide (DMSO, 99.7%), methylammonium iodide (MAI, 99%, Sigma-Aldrich), α-terpineol (90% technical grade, Sigma-Aldrich), titanium (IV) isopropoxide (TTIP, 99%, Sigma-Aldrich), glacial acetic acid (Sigma-Aldrich), graphite powder (<20 μm, synthetic, Sigma-Aldrich), acetylene carbon black (100% compressed, Strem chemicals), titanium dioxide (TiO_2, 90-NRT, Dyesol), lead iodide (PbI_2, 99%, Dyesol), aluminum nitrate nonahydrate (P98.5%, Merck), calcium chloride (P98.0%, Merck), and magnesium acetate tetrahydrate (P99%, Sigma-Aldrich), were used as received.

2.2. Preparation of counter electrodes

Carbon paste (Gr/CB): 0.45 g of graphite flakes and 0.15 g of carbon black powder were mixed together in 10 mL of α-terpineol and ground for 20 min using a mortar and pestle. Then, a TiO_2 precursor consisting of 1 mL of TTIP and 100 μL of glacial acetic acid was added to the mixture before ball-milling for 12 h.

Modified carbon paste (metal-Gr/CB): 0.5 mol% (with respect to the molar concentration of TiO_2) of a metal salt (aluminum nitrate nonahydrate, calcium chloride, or magnesium acetate tetrahydrate) was added to the TiO_2 precursor before adding to the carbon paste. The samples were named according to the metal salts added, *i.e.*, Al-Gr/CB, Ca-Gr/CB, and Mg-Gr/CB.

2.3. Device fabrication

HTM-free *C*-PSCs with an FTO/TiO_2/perovskite/carbon structure were fabricated as follows. Prior to usage, a strip of FTO was etched from the substrate using 2 M HCl and Zn powder. It was then cleaned in an ultrasonic cleaner for 20 min using detergent, deionized water, acetone, 2-propanol, and ethanol in sequence. Next, a TiO_2 precursor solution, consisting of a moderately acidic solution of TTIP and HCL diluted in ethanol, was spin-coated onto the FTO substrate at 3000 r.p.m for 30 s, followed by annealing at 500 °C for 30 min. On top of the compact TiO_2 layer, a mesoporous TiO_2 layer was deposited by spin-coating a TiO_2 paste diluted with ethanol (at a mass ratio of 1:3.5) at 5000 r.p.m for 30 s, followed by heating at 125 °C for 15 min and annealing at 500 °C for 30 min. The perovskite layer was fabricated using a two-step deposition technique. Initially, a 1 M PbI_2 precursor solution (462 mg of PbI_2 dissolved in 800 μL of DMF and 200 μL of DMSO) was deposited by spin-coating at 3000 r.p.m for 30 s and then heated at 70 °C for 30 min. The PbI_2 layer was then coated with carbon paste and dried at 70 °C for 30 min. After drying at room temperature, the film was

submerged in an MAI/2-propanol (1 mg/mL) solution for 30 min to convert PbI_2 to perovskite, after which it was washed with 2-propanol and dried at 70 °C. Fig. S1 depicts the fabrication procedure of HTM-free *C*–PSCs. The entire procedure was conducted under ambient conditions.

2.4. Characterization

Morphological observations and elemental microanalysis of the prepared materials were performed using a field-emission scanning electron microscope (SEM) equipped with an energy-dispersive X-ray spectrometer (EDX). The Gr/CB film thicknesses (~60 μm) were determined using a surface profiler (KLA-tencor). The conductivity of the Gr/CB films was evaluated using a four-point-probe resistivity meter (4 P P, Model DFP-02). The photocurrent density-voltage characteristics of the HTM-free *C*–PSCs were measured using a source-meter (Keithley 2400) under simulated 100 mW/cm^2, AM 1.5G illumination. The active area of the HTM-free *C*–PSCs was 0.3 cm^2. Electrochemical impedance spectroscopy (EIS) measurements were conducted in the dark utilizing an electrochemical workstation (CompactStat.h, Ivium) over a frequency range of 0.1 Hz–1 MHz with a modulation amplitude of 10 mV. The same electrochemical workstation was used to record the current-voltage characteristics of symmetric carbon/perovskite/carbon devices. X-ray photoemission spectroscopy (XPS) and ultraviolet photoelectron spectroscopy (UPS) were performed at BL3.2Ua of the Synchrotron Light Research Institute (SLRI), Thailand. The energies of electrons emitted from the sample were analyzed using a concentric hemispherical analyzer (CLAM2, Thermo VG Scientific) positioned 20° from the surface normal. The binding energy was calibrated to the 284.6 eV C1s maximum.

3. Results and discussion

3.1. Structure of HTM-free C–PSCs

Fig. 1(a) depicts the structural architecture of the HTM-free *C*–PSCs. Each device consists of an FTO substrate, a compact TiO_2 (*c*-TiO_2) layer, a mesoporous TiO_2 (*m*-TiO_2) layer, a perovskite layer, and a carbon layer serving as the CE. The working principle of HTM-free *C*–PSCs is shown in Fig. 1(b). When sunlight is absorbed by the perovskite absorber layer, the generated excitons rapidly dissociate into free electrons and holes due to the low exciton binding energy. The free electrons are then transported through the conduction band of the perovskite to the TiO_2 layer before being collected at the FTO substrate. Meanwhile, the holes are transported through the valence band of the perovskite to the carbon CE. As a result, the perovskite layer functions as both a light harvester and a carrier transport layer.

3.2. SEM and EDX analyses

The cross-sectional SEM image of the completed device (Fig. 2(a)) shows the appropriate orientation of the layers in the following sequence: FTO/TiO_2/perovskite/carbon from bottom to top. As shown in Fig. 2(b), the corresponding EDX mapping confirms the elemental distribution and successful deposition of the various layers. The distribution also reveals that the perovskite layer has infiltrated through the carbon and mesoporous layers. Fig. 2(c–f) display the top SEM images of the Gr/CB and metal-Gr/CB CEs. In the metal-free Gr/CB CE (Fig. 2(c)), the CB nanoparticles are dispersed among larger Gr flakes, forming a network with TiO_2 serving as a binder [31]. The CB nanoparticles function as conductive filler and are also anticipated to bridge gaps between the perovskite layer and the Gr flakes, facilitating interfacial charge transfer. Meanwhile, the larger Gr flakes form longer continuous pathways, thereby enhancing the electrical conductivity of the Gr/CB CEs [32].

Fig. 2(d–f) demonstrate that the addition of metal salts (Al, Ca, and Mg) has no discernible influence on the morphology of the Gr/CB composite. Nevertheless, the EDX spectra shown in Fig. S2(a–d) (Supplementary Material) indicate the presence of trace metal elements in the Gr/CB composite. These observations suggest that the mechanical ball milling reduces the micron-sized metal salt

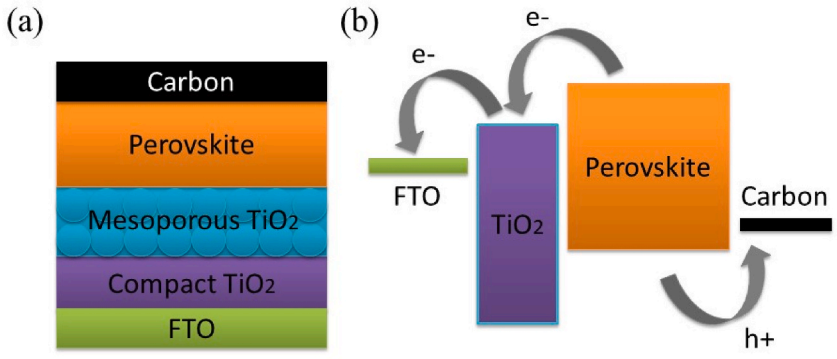

Fig. 1. (a) Schematic diagram and (b) energy band diagram of HTM-free *C*–PSCs.

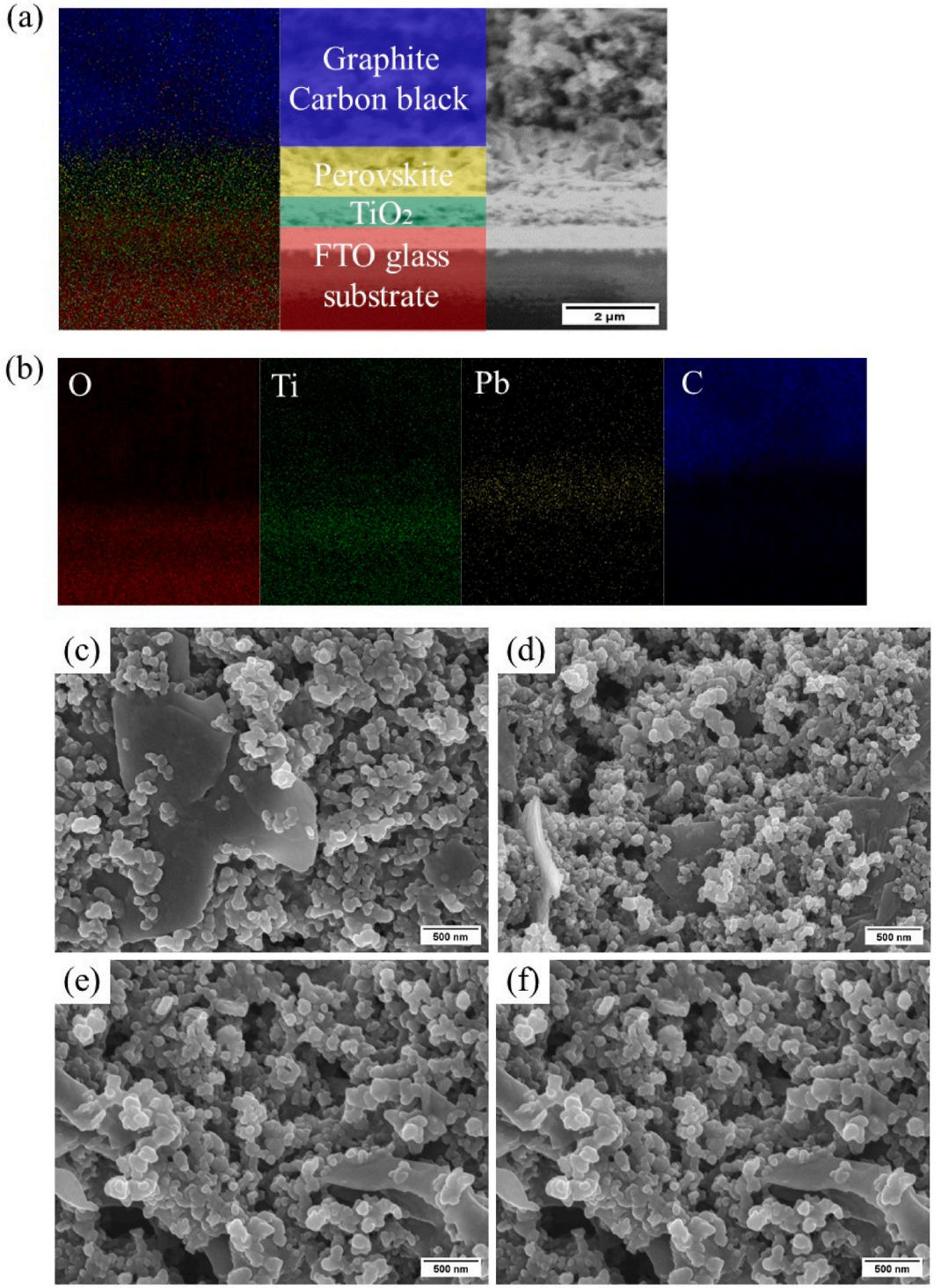

Fig. 2. Cross-sectional SEM image of (a) FTO/TiO_2/perovskite/carbon device and (b) EDX elemental mapping of O, Ti, Pb, and C in the device. The top SEM images of (c) Gr/CB, (d) Al-Gr/CB, (e) Ca-Gr/CB and (f) Mg-Gr/CB CEs.

particles to the nanoscale and uniformly incorporates them throughout the Gr/CB composite. This type of material is differs from commonly used intercalation carbon compounds, where metal ions are inserted between graphite layers [33].

3.3. X-ray diffraction (XRD)

The crystal structures of the components in each layer of the device were characterized using X-ray diffraction (XRD) technique. Fig. 3 displays the XRD patterns for the FTO/TiO_2/Perovskite/Carbon, FTO/TiO_2/Perovskite, FTO/TiO_2/PbI_2 and FTO/TiO_2 films. The study detected diffraction peaks of perovskite at specific 2θ values, namely 14.14°, 19.92°, 23.54°, 24.52°, 28.48°, 31.92°, 34.62°, 40.68°, and 43.16°. These values correspond to the (110), (112), (211), (202), (220), (310), (224), and (314) planes, respectively. The observation of these peaks suggests the emergence of the tetragonal phase of the perovskite [34–36]. The basal (002) diffraction peak of graphite is identifiable by a distinct and pronounced peak at approximately 26.64°. In comparison to the FTO/TiO_2/Perovskite, the FTO/TiO_2 film exhibits a minor peak at 25.5°, which can be assigned to the (101) plane of anatase TiO_2 [37]. The diffraction peaks observed in the sample, specifically those marked with asterisks and occurring at 26.54°, 33.74°, 37.8°, 51.78°, 62.08°, and 65.56°, have been identified as originating from the FTO substrate.

3.4. XPS and UPS analyses

X-ray photoelectron spectroscopy (XPS) was used to establish the surface elemental composition and valence states of the prepared Gr/CB and metal-Gr/CB samples. In the survey XPS spectrum (Fig. 4(a)), carbon, oxygen, titanium, aluminum, calcium, and magnesium signals were detected, indicating the presence of the added Al, Ca, and Mg on the surface of the carbon matrix. Fig. 4(b–d) shows high-resolution C 1s, O 1s, and Ti 2p XPS spectra of Gr/CB, and chemical analyses of the C 1s and O 1s regions for Gr/CB, Al-Gr/CB, Ca-Gr/CB, and Mg-Gr/CB are given in Table S1 (Supplementary Material).

The results depicted in Fig. 4(b) show that the XPS C 1s spectrum consists of four distinct chemically shifted components and can be deconvoluted into the following functional groups: the highest peak at 285.2 eV derives from the sp^2–C hybridized carbon (C–C) atoms,

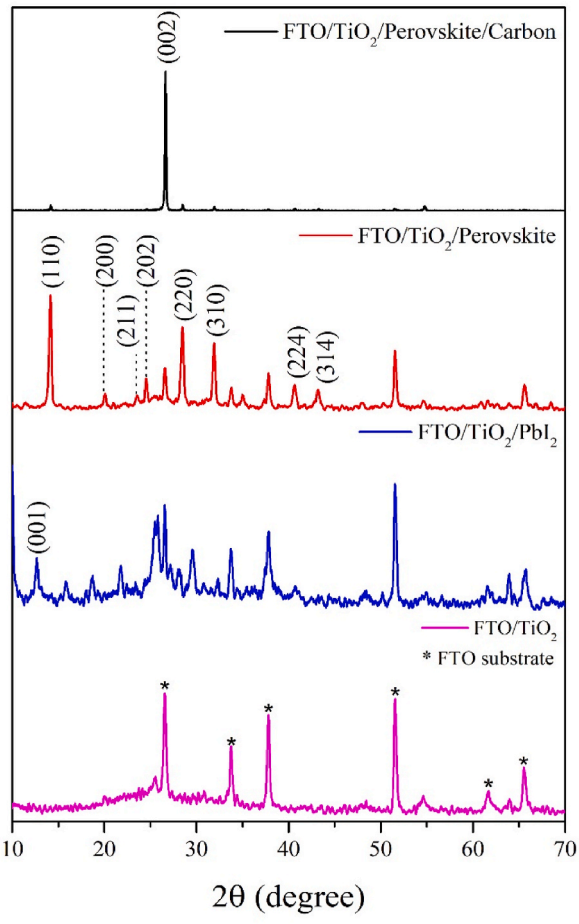

Fig. 3. X-ray diffraction patterns of FTO/TiO_2/Perovskite/Carbon, FTO/TiO_2/Perovskite, FTO/TiO_2/PbI_2 and FTO/TiO_2.

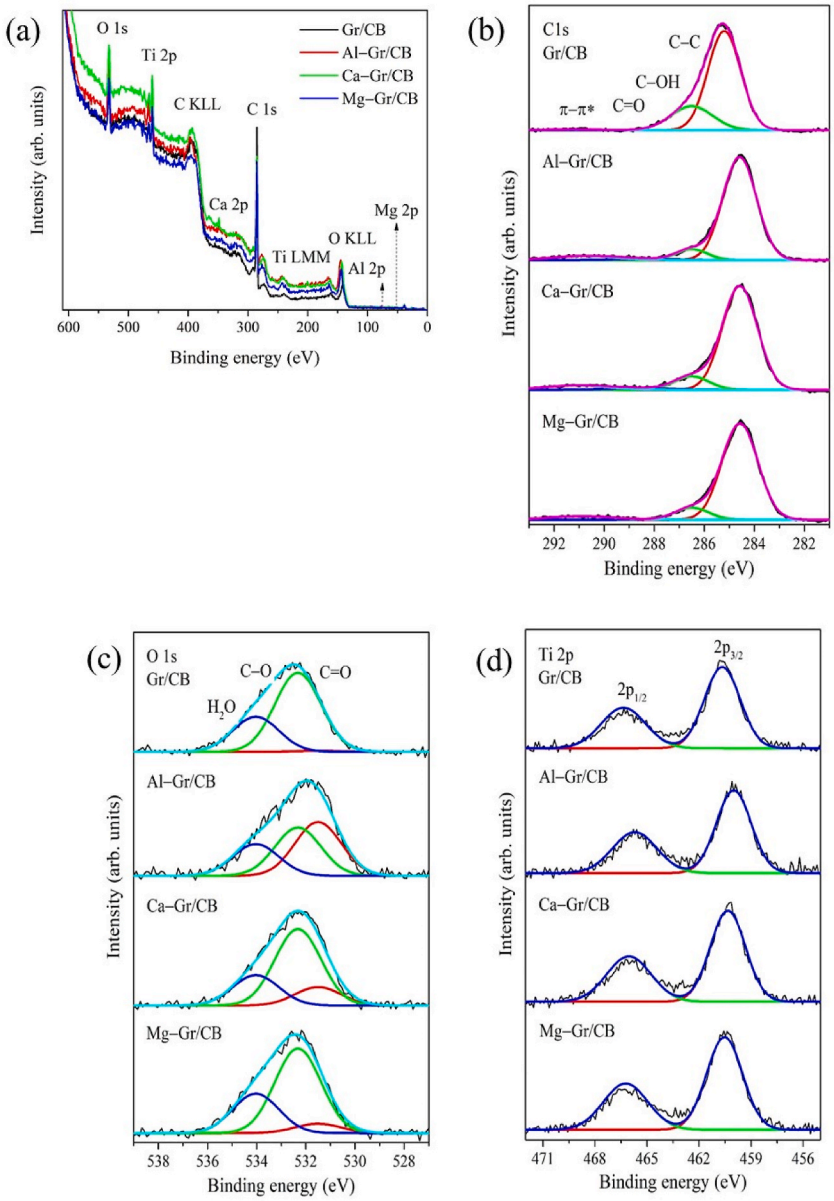

Fig. 4. XPS spectra of Gr/CB, Al-Gr/CB, Ca-Gr/CB, and Mg-Gr/CB composites, displaying the survey scan region (a) and high-resolution spectra of the C 1s (b), O 1s (c), and Ti 2p (d) regions.

followed by three smaller peaks at 286.5 eV, 288.5 eV, and 291.3 eV, which correspond to hydroxyl (C–OH) or epoxy (C–O–C), carbonyl (C═O), and shake-up satellite peaks (π-π*), respectively. XPS reveals that Gr/CB and metal-Gr/CB contain many oxygen-containing functional groups, including C–OH and C═O, which may be conducive to their surface functionalization [38]. According to one previous study, the oxygen-containing groups (C–OH and C═O) on CB might result in Pb–O coordination and the formation of a strong chemical interaction between the perovskite layer and the CB nanoparticles via hydrogen bonding, which would improve quality of the perovskite/carbon CE interface [14]. Consequently, such optimal interfacial contact is expected to reduce the interfacial charge transfer resistance between the perovskite and the CE, thus facilitating hole extraction [39]. Furthermore, the surface oxo species on the carbon may also function as Ti adatom anchoring sites owing to the strong O–Ti interaction [26].

In the O 1s XPS spectra shown in Fig. 4(c), there are three oxygen species with energies of 531.5 eV, 532.3 eV, and 534 eV, respectively. The peak at 531.5 eV is assigned to an OH bond, while the peaks at 532.5 eV and 534 eV arise from C–O bonds and weakly absorbed H_2O, respectively. Fig. 4(d) shows two prominent Ti 2p peaks with binding energies of 460.7 eV (Ti $2p_{3/2}$) and 466.4 eV (Ti $2p_{1/2}$), which correspond to the Ti^{4+} chemical state in TiO_2. This implies that the Ti in Gr/CB and metal-Gr/CB is predominantly in the Ti^{4+} oxidation state. These results also indicate that no Ti^{3+} or Ti^{2+} ions, which are expected to act as trap sites, are present in the

lattice [40]. The XPS spectra shown in Fig. S3(a–c) (Supplementary Material) reveal a single Al 2p peak centered at 74.2 eV for Al-Gr/CB, while in Mg-Gr/CB a single Mg 2p peak is observed at 51.9 eV. On the other hand, the high-resolution Ca 2p spectra of Ca-Gr/CB deconvolved into two peaks at 348.3 eV and 351.8 eV, which correspond to the Ca $2p_{3/2}$ and Ca $2p_{1/2}$ levels.

Ultraviolet photoelectron spectroscopy (UPS) was performed to determine the influence of the added metal salts on the absolute Fermi energy or work function (WF) of the CEs. Fig. 5(a) displays the UPS spectra of the Gr/CB and metal-Gr/CB CEs together with their WFs calculated using $\varphi = h\nu - E_{cutoff}$, where φ is the WF, h is the plank constant, ν is the frequency of the radiation, E_{cutoff} is the cut-off binding energies (secondary edge) from the photon energy (60 eV). An energy level diagram depicting the Gr/CB, Al-Gr/CB, Ca-Gr/CB, and Mg-Gr/CB energy levels relative to those of the other device components is shown in Fig. 5(b).

As shown in Fig. 5(a), the addition of Al, Ca, and Mg to Gr/CB shifts the WF from −4.14 eV (Gr/CB) to −4.59 eV (Al-Gr/CB), −4.32 (Ca-Gr/CB), and −4.28 eV (Mg-Gr/CB), respectively. The lower WF of the metal-Gr/CB CEs is expected to be more favorable than that of the Gr/CB CE for extracting photoinduced holes from the perovskite and in minimizing potential losses [41,42]. This can be explained by the fact that the WF of the metal-Gr/CB is well-matched with the valence band of perovskite, resulting in faster interfacial hole extraction and thus decreased probability of charge recombination before extraction [43].

3.5. Photovoltaic performance

Fig. 6 shows the photocurrent density-voltage (J-V) curves of HTM-free *C*-PSC devices employing Gr/CB, Al-Gr/CB, Ca-Gr/CB, and Mg-Gr/CB CEs under simulated AM 1.5G illumination (100 mW/cm^2), and Table 1 provides a summary of the corresponding photovoltaic parameters. Al-Gr/CB devices exhibit the highest PCE of 9.91%, with an open circuit voltage (V_{oc}) of 0.86 V, short-circuit photocurrent density (J_{sc}) of 23.9 mA/cm^2, and fill factor (FF) of 0.48. The PCEs of the other three devices employing Ca-Gr/CB, Mg-Gr/CB, and Gr/CB CEs were 9.21%, 9.13%, and 8.83%, respectively. Evidently, the Al-Gr/CB devices perform better than the Gr/CB, Ca-Gr/CB, and Mg-Gr/CB devices. This is primarily due to the higher J_{sc} and FF, as well as a modest improvement in V_{oc}. The enhancement of the aforementioned parameters is most likely attributable to the improved hole extraction efficiency and conductivity of the Al-Gr/CB CE, which facilitate both charge transfer and transport while decreasing the probability of charge carrier recombination, thereby increasing the J_{sc}, FF, and Voc [10,43–45]. Table S2 (Supplementary Material) presents the photovoltaic parameters of HTM-free *C*–PSCs utilizing six different devices for sample Al-Gr/CB.

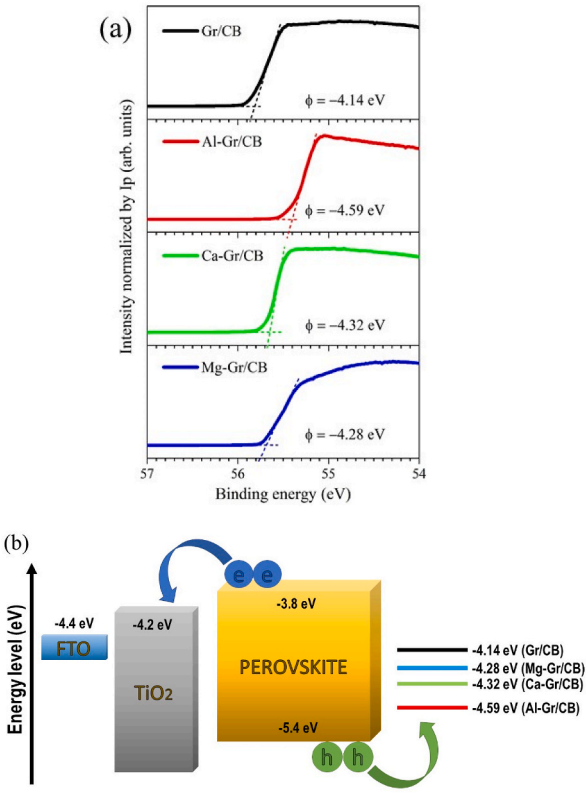

Fig. 5. (a) UPS spectra in the cutoff region of Gr/CB, Al-Gr/CB, Ca-Gr/CB, and Mg-Gr/CB. (b) Schematic illustrating the energy level alignment between the perovskite layer and various CE materials.

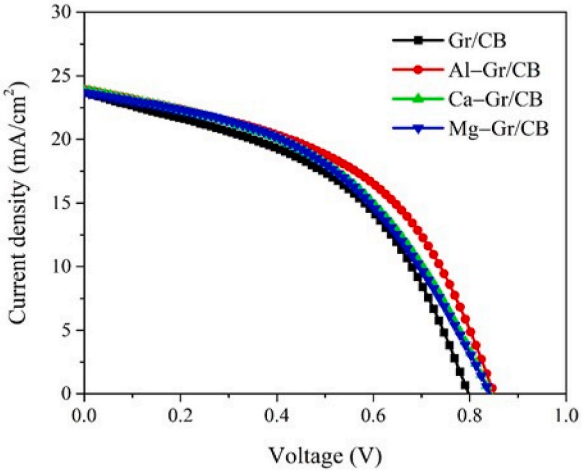

Fig. 6. J-V curves of HTM-free *C*–PSCs employing Gr/CB, Al-Gr/CB, Ca-Gr/CB, and Mg-Gr/CB CEs.

Table 1
Photovoltaic parameters of HTM-free *C*–PSCs employing Gr/CB, Al-Gr/CB, Ca-Gr/CB, and Mg-Gr/CB CEs.

Counter electrode	PCE (%)	V_{oc} (V)	FF	J_{sc} (mA/cm^2)
Gr/CB	8.83	0.80	0.45	23.7
Al-Gr/CB	9.91	0.86	0.48	23.9
Ca-Gr/CB	9.21	0.85	0.46	23.8
Mg-Gr/CB	9.13	0.84	0.46	23.7

3.6. I–V measurements of symmetric cells

To study charge transfer across the perovskite/carbon CE interface, independently of the TiO_2/perovskite and TiO_2/FTO interfaces, the I–V characteristics of carbon/perovskite/carbon in-plane devices prepared with the various metal-Gr/CB materials were examined. As seen in Fig. S4, all devices display a linear dependence of current on bias voltage, showing that all CEs form ohmic contacts with the perovskite layer. The Al-Gr/CB devices exhibit higher currents than the Gr/CB, Ca-Gr/CB, and Mg-Gr/CB devices at any given bias voltage, and this reduced resistance implies better charge transfer across the perovskite/carbon CE interface and/or higher conductivity, which is broadly consistent with the superior photovoltaic parameters of the Al-Gr/CB devices. Consistent with this, the electrical conductivities of the Gr/CB, Al-Gr/CB, Ca-Gr/CB, and Mg-Gr/CB CE films were measured to be 6410 S/m, 6803 S/m, 6614 S/m, and 6460 S/m, respectively, showing that Al-Gr/CB possesses the greatest conductivity of all the CEs tested.

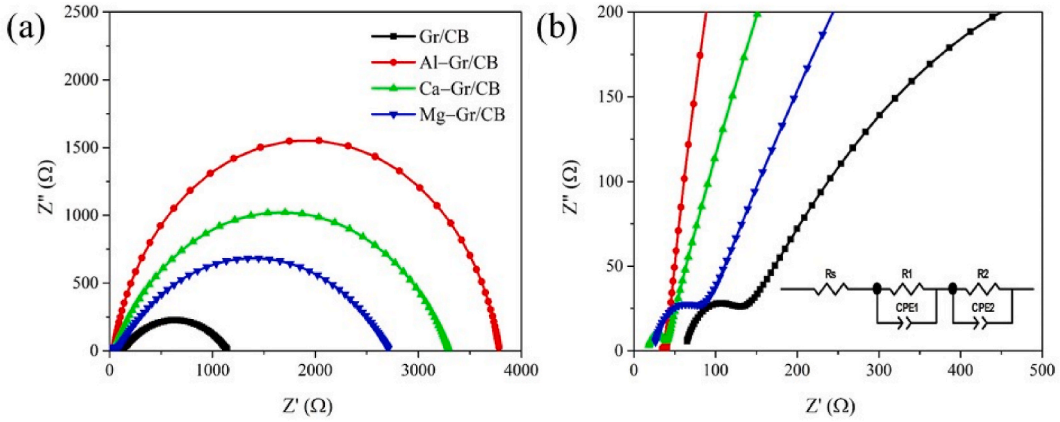

Fig. 7. Nyquist plots of the EIS spectra of HTM-free *C*–PSCs scaled to show the low (a) and high (b) frequency regions. The equivalent circuit used to fit the data is shown in the inset of (b).

3.7. EIS analysis

Electrochemical impedance spectroscopy (EIS) measurements were utilized to further investigate the interfacial charge transfer across the perovskite/carbon interface as well as the recombination behavior of the HTM-free *C*–PSCs. Fig. 7(a) shows the fitted Nyquist plots of the devices based on various metal-Gr/CB CEs, and the corresponding equivalent circuit is shown in the inset of Fig. 7 (b). The spectra were acquired in the dark at a bias voltage of −0.8 V.

The Nyquist plots exhibit two semicircles in two distinct frequency regions that correspond to different processes in the device. The series resistance (R_s) is determined from the magnitude of the impedance in the zero-phase high-frequency region. The semicircle observed in the high-frequency region corresponds to charge transfer between the perovskite layer and the carbon CE with an associated resistance R_1, while the semicircle in the low-frequency region corresponds to charge recombination and accumulation in the perovskite with an associated recombination resistance R_2, which is inversely proportional to the recombination rate. To achieve a higher V_{oc}, a lower recombination rate is required [46]. Compared with the Gr/CB device, the Al-Gr/CB, Ca-Gr/CB, and Mg-Gr/CB devices have significantly lower R_1 in the high-frequency region and higher R_2 in the low-frequency region, especially for the Al-Gr/CB devices. The Al-Gr/CB devices also have lower R_s than the Gr/CB, Ca-Gr/CB, and Mg-Gr/CB devices, resulting in higher FF. The larger R_2 signifies slower interfacial charge recombination, whereas the smaller R_1 indicates faster hole transfer from the perovskite absorber to the carbon CE. Due to the lower R_1, holes can readily flow from the perovskite to the carbon CE. This result is consistent with the J-V measurements, and the superior J_{sc} and FF values can be ascribed to the decreased charge recombination rate [47].

4. Conclusions

In summary, graphite/carbon black composite electrodes incorporating various metal salt additives were fabricated, namely Al-Gr/CB, Ca-Gr/CB, and Mg-Gr/CB. The incorporation of metal salts into the Gr/CB lowered the work function of Gr/CB CE from −4.14 eV to −4.59 eV (Al-Gr/CB), - 4.32 eV (Ca-Gr/CB), and −4.28 eV (Mg-Gr/CB), respectively. Overall, the Al-Gr/CB CE exhibited more favorable energy level alignment between the carbon and perovskite layers than Gr/CB, Ca-Gr/CB, and Mg-Gr/CB, resulting in more effective hole extraction and consequently superior PCE. Devices employing Al-Gr/CB CEs also exhibited slower charge recombination than devices employing other metal-Gr/CB materials, as indicated by analysis of EIS spectra. Taken together, these findings can explain the increased J_{sc}, V_{oc}, and FF of devices based on Al-Gr/CB CEs. This work demonstrates an effective strategy for improving the performance of carbon electrodes in HTM-free *C*–PSCs using a straightforward and cost-effective technique.

Author contribution statement

Muna Fathiah Don: Conceived and designed the experiments; Performed the experiments; Analyzed and interpreted the data; Wrote the paper.

Piyasiri Ekanayake: Conceived and designed the experiments; Analyzed and interpreted the data; Contributed reagents, materials, analysis tools or data; Wrote the paper.

James Robert Jennings: Analyzed and interpreted the data.

Hideki Nakajima: Performed the experiments; Analyzed and interpreted the data.

Udaya Kumar D: Performed the experiments.

Chee Ming Lim: Contributed reagents, materials, analysis tools or data.

Data availability statement

Data included in article/supp. Material/referenced in article.

Declaration of competing interest

The authors declare that they have no known competing financial interests or personal relationships that could have appeared to influence the work reported in this paper.

Acknowledgments

Universiti Brunei Darussalam Research Grant (UBD/RSCH/1.4/FICBF(b)/2022/040) is acknowledged for financial support.

Appendix A. Supplementary data

Supplementary data to this article can be found online at https://doi.org/10.1016/j.heliyon.2023.e17748.

References

[1] L.M. Gonzalez, D. Ramirez, F. Jaramillo, Current status and trends of carbon-based electrodes for fully solution-processed perovskite solar cells, J. Energy Chem. 68 (2022) 222–246, https://doi.org/10.1016/j.jechem.2021.11.020.

[2] D. Li, P. Jiang, W. Zhang, J. Du, C. Qiu, J. Liu, Y. Hu, Y. Rong, A. Mei, H. Han, Series resistance modulation for large-area fully printable mesoscopic perovskite solar cells, Sol. RRL. 6 (2022), https://doi.org/10.1002/solr.202100554.

[3] Y. Chen, S. Wu, X. Li, M. Liu, Z. Chen, P. Zhang, S. Li, Efficient and stable low-cost perovskite solar cells enabled by using surface passivated carbon as the counter electrode, J. Mater. Chem. C 10 (2022) 1270–1275, https://doi.org/10.1039/d1tc05351e.

[4] Z. Shi, S. Li, C. Min, J. Xie, R. Ma, Modification of energy levels by cetyltrimethylammonium bromide at the perovskite/carbon interface for highly efficient and stable perovskite solar cells, Org. Electron. 112 (2022), 106689, https://doi.org/10.1016/j.orgel.2022.106689.

[5] D. Bogachuk, S. Zouhair, K. Wojciechowski, B. Yang, V. Babu, L. Wagner, B. Xu, J. Lim, S. Mastroianni, H. Pettersson, A. Hagfeldt, A. Hinsch, Low-temperature carbon-based electrodes in perovskite solar cells, Energy Environ. Sci. 13 (2020) 3880–3916, https://doi.org/10.1039/d0ee02175j.

[6] V. Babu, R. Fuentes Pineda, T. Ahmad, A.O. Alvarez, L.A. Castriotta, A. Di Carlo, F. Fabregat-Santiago, K. Wojciechowski, Improved stability of inverted and flexible perovskite solar cells with carbon electrode, ACS Appl. Energy Mater. 3 (2020) 5126–5134, https://doi.org/10.1021/acsaem.0c00702.

[7] S. Bhandari, A. Roy, A. Ghosh, T.K. Mallick, S. Sundaram, Performance of WO3-incorporated carbon electrodes for ambient mesoscopic perovskite solar cells, ACS Omega 5 (2020) 422–429, https://doi.org/10.1021/acsomega.9b02934.

[8] D. Papadatos, D. Sygkridou, E. Stathatos, Carbon-based, novel triple cation mesoscopic perovskite solar cell fabricated entirely under ambient air conditions, Mater. Lett. 268 (2020), https://doi.org/10.1016/j.matlet.2020.127621.

[9] A.C. Nkele, A.C. Nwanya, N.U. Nwankwo, R.U. Osuji, A.B.C. Ekwealor, P.M. Ejikeme, M. Maaza, F.I. Ezema, Investigating the properties of nano nest-like nickel oxide and the NiO/Perovskite for potential application as a hole transport material, Adv. Nat. Sci. Nanosci. Nanotechnol. 10 (2019), https://doi.org/10.1088/2043-6254/ab5102.

[10] I. Jeon, A. Shawky, S. Seo, Y. Qian, A. Anisimov, E.I. Kauppinen, Y. Matsuo, S. Maruyama, Carbon nanotubes to outperform metal electrodes in perovskite solar cellsviadopant engineering and hole-selectivity enhancement, J. Mater. Chem. A. 8 (2020) 11141–11147, https://doi.org/10.1039/d0ta03692g.

[11] D. Bogachuk, B. Yang, J. Suo, D. Martineau, A. Verma, S. Narbey, M. Anaya, K. Frohna, T. Doherty, D. Muller, J.P. Herterich, S. Zouhair, A. Hagfeldt, S. D. Stranks, U. Wurfel, A. Hinsch, L. Wagner, Perovskite solar cells with carbon-based electrodes – quantification of losses and strategies to overcome them, Adv. Energy Mater. 12 (2022), https://doi.org/10.1002/aenm.202103128.

[12] R. He, X. Huang, M. Chee, F. Hao, P. Dong, Carbon-based perovskite solar cells: from single-junction to modules, Carbon Energy 1 (2019) 109–123, https://doi.org/10.1002/cey2.11.

[13] S. Zhu, J. Tian, J. Zhang, C. Gao, X. Liu, Improving the interfacial contact of screen-printed carbon electrodes for perovskite solar cells, ACS Appl. Energy Mater. 4 (2021) 5554–5559, https://doi.org/10.1021/acsaem.1c00232.

[14] C. Tian, A. Mei, S. Zhang, H. Tian, S. Liu, F. Qin, Y. Xiong, Y. Rong, Y. Hu, Y. Zhou, S. Xie, H. Han, Oxygen management in carbon electrode for high-performance printable perovskite solar cells, Nano Energy 53 (2018) 160–167, https://doi.org/10.1016/j.nanoen.2018.08.050.

[15] M.F. Don, P. Ekanayake, J.R. Jennings, H. Nakajima, C.M. Lim, Graphite/carbon black counter electrode deposition methods to improve the efficiency and stability of hole-transport-layer-free perovskite solar cells, ACS Omega (2022), https://doi.org/10.1021/acsomega.2c02555.

[16] S. Pitchaiya, N. Eswaramoorthy, M. Natarajan, A. Santhanam, V. Asokan, V. Madurai Ramakrishnan, B. Rangasamy, S. Sundaram, P. Ravirajan, D. Velauthapillai, Perovskite solar cells: a porous graphitic carbon based hole transporter/counter electrode material extracted from an invasive plant species Eichhornia crassipes, Sci. Rep. 10 (2020), https://doi.org/10.1038/s41598-020-62900-4.

[17] M. Guo, J. Liu, Y. Yuan, Z. Zhang, S. Yin, J. Leng, N. Huang, CNTs/Cf based counter electrode for highly efficient hole-transport-material-free perovskite solar cells, J. Photochem. Photobiol. Chem. 403 (2020), https://doi.org/10.1016/j.jphotochem.2020.112843.

[18] C. Zhang, Y. Luo, X. Chen, Y. Chen, Z. Sun, S. Huang, Effective improvement of the photovoltaic performance of carbon-based perovskite solar cells by additional solvents, Nano-Micro Lett. 8 (2016) 347–357, https://doi.org/10.1007/s40820-016-0094-4.

[19] J. Zhou, J. Wu, N. Li, X. Li, Y.Z. Zheng, X. Tao, Efficient all-air processed mixed cation carbon-based perovskite solar cells with ultra-high stability, J. Mater. Chem. A. 7 (2019) 17594–17603, https://doi.org/10.1039/c9ta05744g.

[20] N. Zhang, Y. Guo, X. Yin, M. He, X. Zou, Spongy carbon film deposited on a separated substrate as counter electrode for perovskite-based solar cell, Mater. Lett. 182 (2016) 248–252, https://doi.org/10.1016/j.matlet.2016.07.004.

[21] D. Bogachuk, R. Tsuji, D. Martineau, S. Narbey, J.P. Herterich, L. Wagner, K. Suginuma, S. Ito, A. Hinsch, Comparison of highly conductive natural and synthetic graphites for electrodes in perovskite solar cells, Carbon N. Y. 178 (2021) 10–18, https://doi.org/10.1016/j.carbon.2021.01.022.

[22] S.K. Yadav, Hydrophobic compressed carbon/graphite based long-term stable perovskite solar cells, Mater. Chem. Phys. 268 (2021), https://doi.org/10.1016/j.matchemphys.2021.124709.

[23] P. Jiang, Y. Xiong, M. Xu, A. Mei, Y. Sheng, L. Hong, T.W. Jones, G.J. Wilson, S. Xiong, D. Li, Y. Hu, Y. Rong, H. Han, The influence of the work function of hybrid carbon electrodes on printable mesoscopic perovskite solar cells, J. Phys. Chem. C 122 (2018) 16481–16487, https://doi.org/10.1021/acs.jpcc.8b02163.

[24] M. Duan, C. Tian, Y. Hu, A. Mei, Y. Rong, Y. Xiong, M. Xu, Y. Sheng, P. Jiang, X. Hou, X. Zhu, F. Qin, H. Han, Boron-doped graphite for high work function carbon electrode in printable hole-conductor-free mesoscopic perovskite solar cells, ACS Appl. Mater. Interfaces 9 (2017) 31721–31727, https://doi.org/10.1021/acsami.7b05689.

[25] X. Zheng, H. Chen, Q. Li, Y. Yang, Z. Wei, Y. Bai, Y. Qiu, D. Zhou, K.S. Wong, S. Yang, Boron doping of multiwalled carbon nanotubes significantly enhances hole extraction in carbon-based perovskite solar cells, Nano Lett. 17 (2017) 2496–2505, https://doi.org/10.1021/acs.nanolett.7b00200.

[26] C. Zhang, S. Liang, W. Liu, F.T. Eickemeyer, X. Cai, K. Zhou, J. Bian, H. Zhu, C. Zhu, N. Wang, Z. Wang, J. Zhang, Y. Wang, J. Hu, H. Ma, C. Xin, S. M. Zakeeruddin, M. Gratzel, Y. Shi, Ti1–graphene single-atom material for improved energy level alignment in perovskite solar cells, Nat. Energy 6 (2021) 1154–1163, https://doi.org/10.1038/s41560-021-00944-0.

[27] C. Liu, C. Gao, W. Wang, X. Wang, Y. Wang, W. Hu, Y. Rong, Y. Hu, L. Guo, A. Mei, H. Han, Cellulose-based oxygen-rich activated carbon for printable mesoscopic perovskite solar cells, Sol. RRL. 5 (2021), https://doi.org/10.1002/solr.202100333.

[28] M. Wu, M. Sun, H. Zhou, J.Y. Ma, T. Ma, Carbon counter electrodes in dye-sensitized and perovskite solar cells, Adv. Funct. Mater. 30 (2020), https://doi.org/10.1002/adfm.201906451.

[29] M. Chen, R.H. Zha, Z.Y. Yuan, Q.S. Jing, Z.Y. Huang, X.K. Yang, S.M. Yang, X.H. Zhao, D.L. Xu, G.D. Zou, Boron and phosphorus co-doped carbon counter electrode for efficient hole-conductor-free perovskite solar cell, Chem. Eng. J. 313 (2017) 791–800, https://doi.org/10.1016/j.cej.2016.12.050.

[30] M. Guo, C. Wei, C. Liu, K. Zhang, H. Su, K. Xie, P. Zhai, J. Zhang, L. Liu, Composite electrode based on single-atom Ni doped graphene for planar carbon-based perovskite solar cells, Mater. Des. 209 (2021), https://doi.org/10.1016/j.matdes.2021.109972.

[31] M.F. Don, P. Ekanayake, H. Nakajima, A.H. Mahadi, C.M. Lim, Improvement of dye-sensitized solar cell performance through introducing TiO2 in acetylene carbon black-graphite composite electrode, Thin Solid Films (2020) 706, https://doi.org/10.1016/j.tsf.2020.138042.

[32] M.F. Don, P. Ekanayake, H. Nakajima, A.H. Mahadi, C.M. Lim, A. Atod, Acetylene carbon black-graphite composite as low-cost and efficient counter electrode for dye-sensitized solar cells (DSSCs), Ionics 25 (2019) 5585–5593, https://doi.org/10.1007/s11581-019-03071-9.

[33] W. Wei, Y.H. Hu, Highly conductive Na-embedded carbon nanowalls for hole-transport-material-free perovskite solar cells without metal electrodes, J. Mater. Chem. A. 5 (2017) 24126–24130, https://doi.org/10.1039/c7ta07730k.

[34] E. Arkan, M. Unal, E. Yalcin, M.Z. Yigit Arkan, S. Yurtdas, M. Can, C. Tozlu, S. Demic, Influence of end groups variation of self assembled monolayers on performance of planar perovskite solar cells by interface regulation, Mater. Sci. Semicond. Process. 123 (2021), https://doi.org/10.1016/j.mssp.2020.105514.

[35] K. Li, H. Chen, H. Liu, Y. Yuan, Y. Gao, B. Yang, C. Zhou, Dependence of power conversion properties of the hole-conductor-free mesoscopic perovskite solar cells on the thickness of carbon film, Org. Electron. 62 (2018) 298–303, https://doi.org/10.1016/j.orgel.2018.08.013.

[36] D.I. Kim, J.W. Lee, R.H. Jeong, J.H. Boo, A high-efficiency and stable perovskite solar cell fabricated in ambient air using a polyaniline passivation layer, Sci. Rep. 12 (2022), https://doi.org/10.1038/s41598-021-04547-3.

[37] W. Chen, X. Yin, M. Que, H. Xie, J. Liu, C. Yang, Y. Guo, Y. Wu, W. Que, A comparative study of planar and mesoporous perovskite solar cells with printable carbon electrodes, J. Power Sources 412 (2019) 118–124, https://doi.org/10.1016/j.jpowsour.2018.11.031.
[38] H. Hou, L. Shao, Y. Zhang, G. Zou, J. Chen, X. Ji, Large-area carbon nanosheets doped with phosphorus: a high-performance anode material for sodium-ion batteries, Adv. Sci. 4 (2017), https://doi.org/10.1002/advs.201600243.
[39] J. Yan, S. Lin, X. Qiu, H. Chen, K. Li, Y. Yuan, M. Long, B. Yang, Y. Gao, C. Zhou, Accelerated hole-extraction in carbon-electrode based planar perovskite solar cells by moisture-assisted post-annealing, Appl. Phys. Lett. 114 (2019), https://doi.org/10.1063/1.5087098.
[40] N. Narudin, P. Ekanayake, Y.W. Soon, H. Nakajima, C.M. Lim, Enhanced properties of low-cost carbon black-graphite counter electrode in DSSC by incorporating binders, Sol. Energy 225 (2021) 237–244, https://doi.org/10.1016/j.solener.2021.06.070.
[41] J.W. Lee, I. Jeon, H.S. Lin, S. Seo, T.H. Han, A. Anisimov, E.I. Kauppinen, Y. Matsuo, S. Maruyama, Y. Yang, Vapor-Assisted ex-situ doping of carbon nanotube toward efficient and stable perovskite solar cells, Nano Lett. 19 (2019) 2223–2230, https://doi.org/10.1021/acs.nanolett.8b04190.
[42] X. Zheng, H. Chen, Q. Li, Y. Yang, Z. Wei, Y. Bai, Y. Qiu, D. Zhou, K.S. Wong, S. Yang, Boron doping of multiwalled carbon nanotubes significantly enhances hole extraction in carbon-based perovskite solar cells, Nano Lett. 17 (2017) 2496–2505, https://doi.org/10.1021/acs.nanolett.7b00200.
[43] Y. Zhu, S. Jia, J. Zheng, Y. Lin, Y. Wu, J. Wang, Facile synthesis of nitrogen-doped graphene frameworks for enhanced performance of hole transport material-free perovskite solar cells, J. Mater. Chem. C 6 (2018) 3097–3103, https://doi.org/10.1039/c8tc00086g.
[44] J. Han, X. Yin, Y. Zhou, H. Nan, Y. Gu, M. Tai, J. Li, H. Lin, High efficient large-area perovskite solar cells based on paintable carbon electrode with nio nanocrystal-carbon intermediate layer, Chem. Lett. 48 (2019) 734–737, https://doi.org/10.1246/cl.190210.
[45] C. Wu, K. Wang, Y. Jiang, D. Yang, Y. Hou, T. Ye, C.S. Han, B. Chi, L. Zhao, S. Wang, W. Deng, S. Priya, All electrospray printing of carbon-based cost-effective perovskite solar cells, Adv. Funct. Mater. 31 (2021), https://doi.org/10.1002/adfm.202006803.
[46] L. Wang, G.R. Li, Q. Zhao, X.P. Gao, Non-precious transition metals as counter electrode of perovskite solar cells, Energy Storage Mater. 7 (2017) 40–47, https://doi.org/10.1016/j.ensm.2016.11.007.
[47] L. Wang, G.R. Li, Q. Zhao, X.P. Gao, Non-precious transition metals as counter electrode of perovskite solar cells, Energy Storage Mater. 7 (2017) 40–47, https://doi.org/10.1016/j.ensm.2016.11.007.